Niche-guided tissue patterning by chemomechanical flow lithography

Peter L. H. Newman*[1], Pierre Osteil[2,3], Tim A. Anderson[1], Jane Q. J. Sun[2,3], Daryan Kempe[4], Maté Biro[4], Patrick P.L. Tam[2,3], Jae-Won Shin[5], Hala Zreiqat*[1]

[1] ARC Training Centre for Innovative Bioengineering, The University of Sydney, Sydney, Australia.
[2] Embryology Unit, Children's Medical Research Institute, Sydney, Australia
[3] School of Medical Science, Faculty of Medicine and Health, The University of Sydney
[4] EMBL Australia, Single Molecule Science Node, School of Medical Sciences, UNSW, Sydney, Australia.
[5] Department of Pharmacology and Regenerative Medicine; Department of Bioengineering, University of Illinois at Chicago, Illinois, USA

*Corresponding authors, Peter Newman: p.newman@sydney.edu.au, Hala Zreiqat: hala.zreiqat@sydney.edu.au

Pluripotent-stem-cell-derived tissue-models have been established with increasingly physiological shape, size and function[1–3]. However, the histogenic and morphogenetic processes present in these models proceed stochastically. This reflects an absence of technologies able to produce complex supportive cell niches that can reproducibly guide tissue patterning and generate well-defined tissue structures. To address this, we have developed chemomechanical flow lithography (CMFL), a printing technology that delivers orthogonally programmable chemical and mechanical properties to microstructured niches that drive the differentiation of selective cell types and spatial emplacement of these cells in a micropattern. We print microstructured niches conjugated with peptides, proteins and macromolecular morphogens across a range of Young's moduli. Using such niches, we generated tissue patterned constructs from a single cell source with regionalised cell differentiation, including a bone-fat osteoid from stromal mesenchyme, and a patterned assembly of germ-layer tissues derived from pluripotent stem cells. Thus, CMFL is a valuable tool for generating orthogonally and chemomechanically defined niches able to guide spatially defined tissue patterns. This approach enables studies to better understand how extrinsic niche factors regulate histogenic and morphogenetic processes, towards engineering complex structured tissue and organ systems with higher-level emergent function.

Generating *ex vivo* tissue of biologically relevant architecture and physiologically compatible functions remains a key challenge of tissue engineering. While significant progress has been made generating tissue models of increasing complexity[1–6], current approaches are constrained by the use of homogeneous extracellular environments that limit formation of the structural diversity and the acquisition of higher-level cellular functions. One approach to overcome this limitation is to support cells with synthetic microstructured niches able to guide local tissue interaction and generate tissue-typic and organotypic entities. To this end, researchers have developed biomaterials

1

with properties that mimic the mechanics[7–9] and chemistry[10–14] of the cell niche. By engineering these properties, such synthetic niche materials can elicit specific cell responses that if appropriately structured could support tissue with more recapitulative architecture and function. However, there are no existing technologies shown to generate microstructured environment with well-defined chemomechanical properties able to guide tissue patterning and generate multilineage cell constructs in which selective cell types are assembled with reproducible spatial patterning.

One promising technology to generate synthetic niches with microstructured properties is 3D printing. In the field of biomaterials, a common printing method involves extrusion of a biopolymer ink or the direct extrusion of cells. Extrusion printers can produce materials with discrete properties through the sequential extrusion of different materials, either from separate print cartridges each loaded with different bioinks[15–19], or through mixing solutions prior to their extrusion through a single nozzle[20,21]. Using this approach researchers have demonstrated the structuring of differing cell types[3,18] mechanical properties[17,21] and biochemicals[22]. Structured materials that are fabricated with extrusion printing are limited in the number of differing material types by the number of print cartridges or their ability to efficiently switch and mix solutions within a single print cartridge. Accordingly, the demonstration of structured biomaterial systems fabricated from extrusion printing has been limited to a no more than 4 materials[19] and is yet to demonstrate functionally graded properties[20] with comparable resolutions to those possible through photolithographic methods[23]. These limitations make the extrusion approach problematic for fabricating cell niche materials that requires subcellular scale features with orthogonally programmable chemomechanical microstructural material cues. As an alternative approach to generating structured tissue systems using microstructured cues from cell niche environments, organoid models have been generated using direct embedded printing of hiPSCs[3,24,25]. Therein, iPSCs can be directly extruded or embedded into defined architectures and subsequently differentiated via external media-derived cues or intercellular feedback from concurrently patterned differentiated cells. While this approach has been shown to be permissive to generating larger macroscale organoids with improved reproducibility, these models still rely on the stochastic histogenic processes during hiPSCs self-organisation.

Photolithography is alternative printing method that uses light to selectively polymerise a material from a photoresin. This method offers technical solutions to some of the obstacles faced when extrusion-printing complex materials. For example, photolithographic printing methods have generated materials with nanoscale features of 30 nm[26], a feat yet to be achieved using extrusion-printing. Early work developing heterogeneous biomaterials with chemically discrete properties used photolithography to pattern regions of small bioactive molecules and peptides[27–29], though

2

since then, methods for the discrete spatiotemporal structuring of sensitive and complex biomacromolecules have been developed[30], as well as methods for printing materials with discrete mechanical properties[31]. Using photolithography, materials with discrete properties can be printed by changing the composition of a photoresin solution during printing. In practice, this can be done with the serial injection of multiple photoresins with variable composition[32]. These photoresins flow through the polymerisation volume, which gives this method the name flow lithography (FL). The FL method has been widely used in microfluidics to fabricate microparticles[33]. FL overcomes the technical hurdles of extrusion methods by using separate subsystems for solution injection, mixing and placement/polymerization. Thus, for FL printing, materials with structured properties can be fabricated with a resolution primarily limited by the focus of light, the so called 'spot-size'. While photolithographic approaches have generated heterogeneous microstructured niches able to differentially regulate simple cell functions, such as cell attachment[29,34] and proliferation[30], the use of microstructured properties to spatially regulate more complex cell functions including mechanosensing, directing cell fate, and structuring multilineage differentiations remains unexplored.

Here we demonstrated chemomechanical flow lithography (CMFL), a technology for fabricating orthogonally programmable chemically and mechanically microstructured hydrogels that can provide niche cues to guide reproducible multilineage tissue patterning. To achieve this, we developed a printer and photoresin system with tunable chemomechanical properties that can conjugated with peptides, proteins and morphogens across a range of physiologically relevant Young's moduli. We explore the use of orthogonally defined chemomechanical niche cues for the microscale regulation of cell functions that underpin tissue patterning, including mechanosensing and the differentiation of selective cell types. This enables the rational design of niche-derived multilineage cell constructs with controlled tissue patterning and of reproducible structure, including a bone-fat tissue construct that mimics the osteon and a mechanically polarised germ-layer tissue. Thus, CMFL is a powerful tool for tissue engineering well defined tissue constructs from chemomechanically structured cell niches.

Results

Chemomechanical flow lithography for orthogonal programming of niches with chemomechanically defined microstructure.

CMFL builds on photolithographic approaches to generate printed materials with microstructured mechanics and chemistry[27–29]. Using CMFL, complex materials are generated by flowing photoresins through a print chamber during printing, hence the name flow lithography (**Fig. 1**, **Fig. S1,2**). The resolution and size of printed structures is then controlled by changing the

3

focus of the laser within the print chamber, with resolutions demonstrated at ~7 µm (**Fig. 1b-1, Fig. S3**). Together with the CMFL printer, we use a photoresin composed of an inert hydrogel monomer (polyethylene glycol diacrylate), a photoinitiator (lithium phenyl-2,4,6-trimethylbenzoylphosphinate or LAP[35]) and peptides, proteins and morphogens with a free thiol

110   functional group available from cysteine peptide moieties (**Fig. 1c**). When the photoinitiator is excited by the laser, the hydrogel monomer polymerises alongside a thiol-ene bioconjugation reaction that covalently crosslinks biochemicals to the otherwise bioinert niches. Accordingly, material bioactivity is specified by changing the concentration of biochemical additives with free cysteine moieties (**Fig. 1b-5,6, Fig. S4**). Likewise, 3D printed materials with varied mechanics can

115   be achieved by changing the concentration of the monomer and photoinitiator, achieving physiologically stiff (**Fig. 1b-4 Fig. 1f**) and soft (**Fig. 1b-5, Fig. 1g**) Young's moduli. Scaffolds with varied 3D architectures can be printed and seeded with cells (**Fig. 1 h,i**).
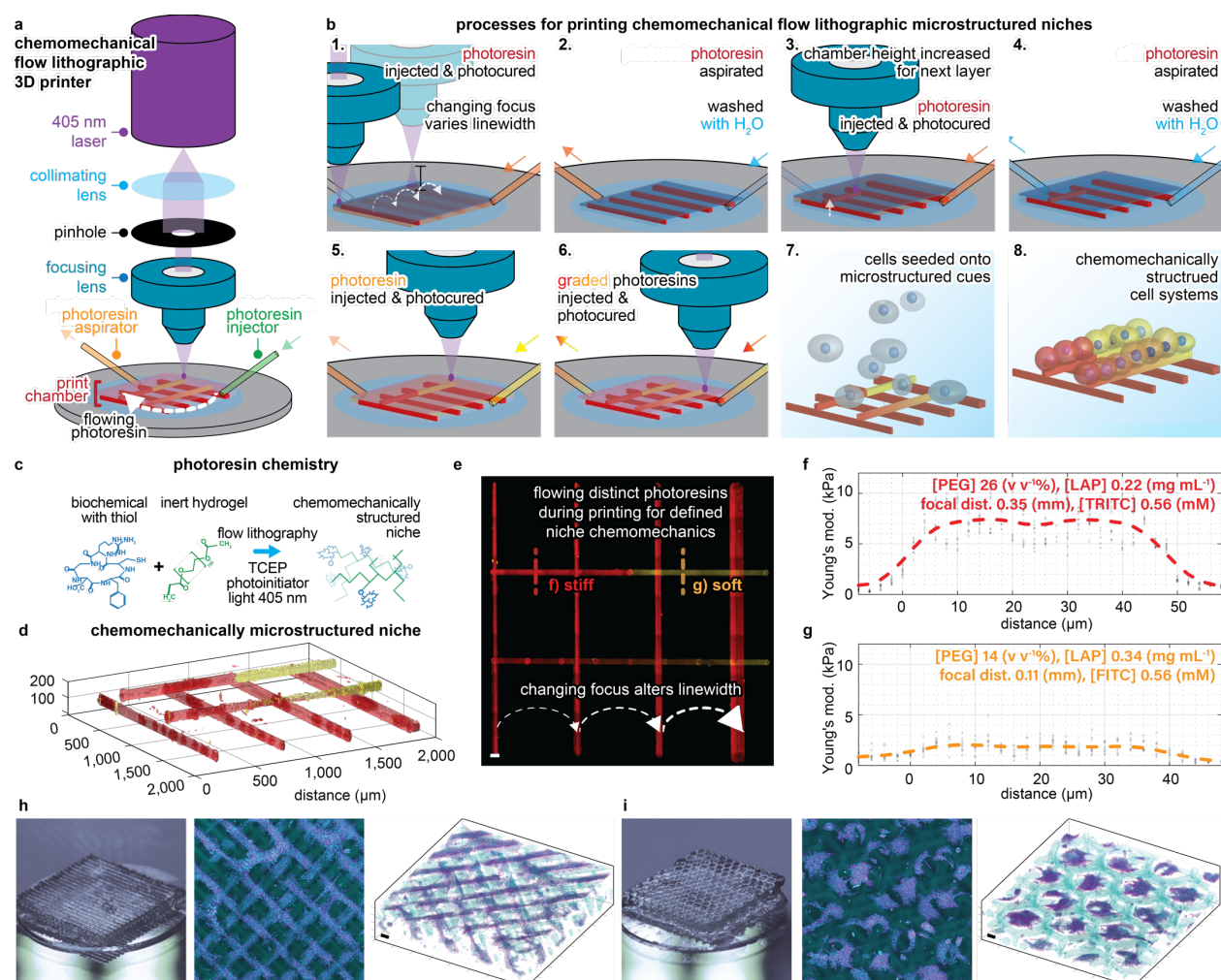

Fig. 1 | Chemomechanical flow lithography for fabricating microstructured niches. a, Components of the CMFL 3D printer.

120   b, Stepwise fabrication processes to generate cell niches with complex structured chemomechanical microproperties. c, Photoresin chemistry used. d, Confocal image of a CMFL niche with complex properties, including changes to linewidth, mechanics (Young's modulus) and chemical microproperties (concentration of the fluorophores FITC and TRITC). e, Maximum intensity projection of the CMFL niche confocal data, scale bar 50 µm. Dotted red and orange lines annotate the profile of force spectroscopy in f,g.

4

Young's modulus across filaments of the pictured niches. Fabrication variables are shown at the top of the graphs for physiologically f stiff (7.5 kPa, red, TRITC) and g soft (2.5 kPa, orange, FITC) segments. Actin (magenta) and nuclear (cyan) stained ADSCs cultured over CMFL printed 3D scaffolds with h, 'stacked-logs' or i, 'offset-honeycomb-layers' architecture. Macro lens photography is show with maximum intensity projections and 3D renders, scale bars 200 µm.

To print specific niche properties, we required empirical data relating the independent fabrication variables to the printed linewidth, mechanics and chemical properties. We characterised six variables that affect niche properties, including three variables controlled by the printer (laser scan velocity, focus and laser power) and three photoresin solution variables (the concentration of photoinitiator, monomer and bioconjugate Biotin-PEG-SH, a model biochemical with free thiol group) (**Fig. 2 a-f**). Decreased light exposure (**Fig. 2a,b**), photoinitiator (**Fig. 2d**), and monomer concentrations (**Fig. 2e**) decreased both Young's modulus and the linewidth of prints, consistent with a lowered rate of polymerization due to the decreased light absorption and consequentially lower photoinitiator free radical dissociation and monomer conversion (see notes on photopolymerization in the supplementary information, **Fig. S5-6**). As a function of the focus, changes to the linewidth were approximated with a linear function that correlated with the diameter of the conic angle of laser transmittance (**Fig. 2c**). Additionally, we characterised the effect of changing the concentration of Biotin-PEG-SH, a model biochemical with a free thiol group, on both Young's modulus and the linewidth of CMFL materials (**Fig. 2f**). We demonstrated that for conjugation of up to 8 mM, there were no significant changes in the resulting Young's modulus or linewidth.

A simplified variable state-space was then chosen to minimise the number of independent printing variables while still exhibiting physiologically relevant properties (**Fig. 2g–i**). Accordingly, we fixed the laser scan velocity to 100 mm min^{-1} and laser power to 100%, as well as unified the two variables of photoinitiator and monomer concentration to a single variable by changing the concentration of one as a function of the other (Methods, Equation 2). These simplifications left a state-space with the three independent variables of focus, bioconjugate concentration and the combined concentration of photoinitiator–monomer. The characterisation and interpolation within this variable state-space allowed printing of niches with well-defined properties (**Fig. 2g-i**, see methods for additional details). To demonstrate property orthogonality, we printed niches with adjacent structures of either increasing or decreasing relative Young's moduli, linewidth and relative bioconjugate fluorescence (**Fig. S7**). Further, we also demonstrated the CMFL 3DP method is not limited to changes in the concentrations of monomer or conjugates but can also be used for changes to the concentration of embedded cells, including the generation of microstructures with gradients of different cell types simultaneously changing concentration in

5

orthogonal directions (**Fig. S8**). This method allowed the empirical specification of orthogonally programmable chemomechanically defined microstructured niches using a state-space with the shown physiological properties.
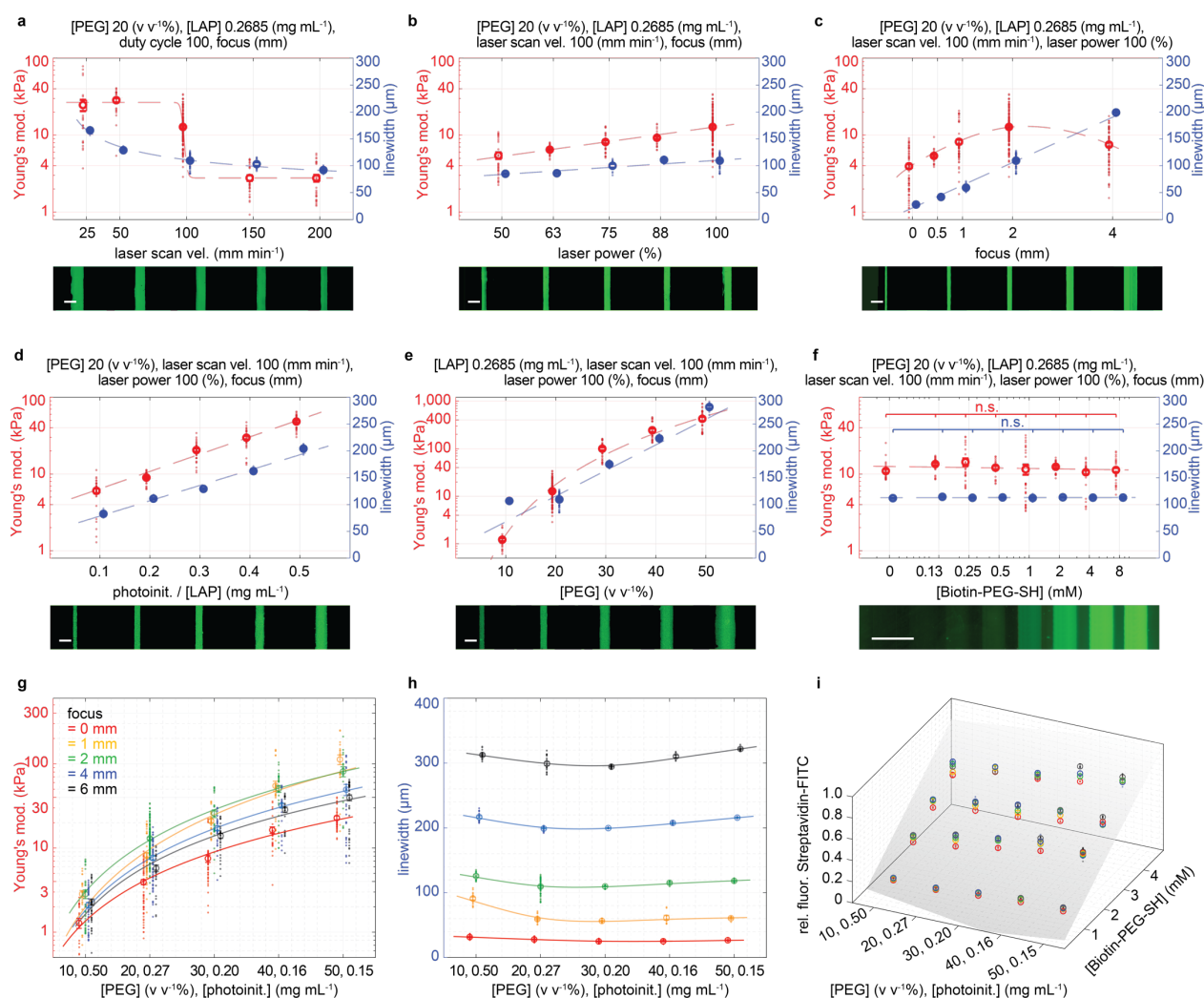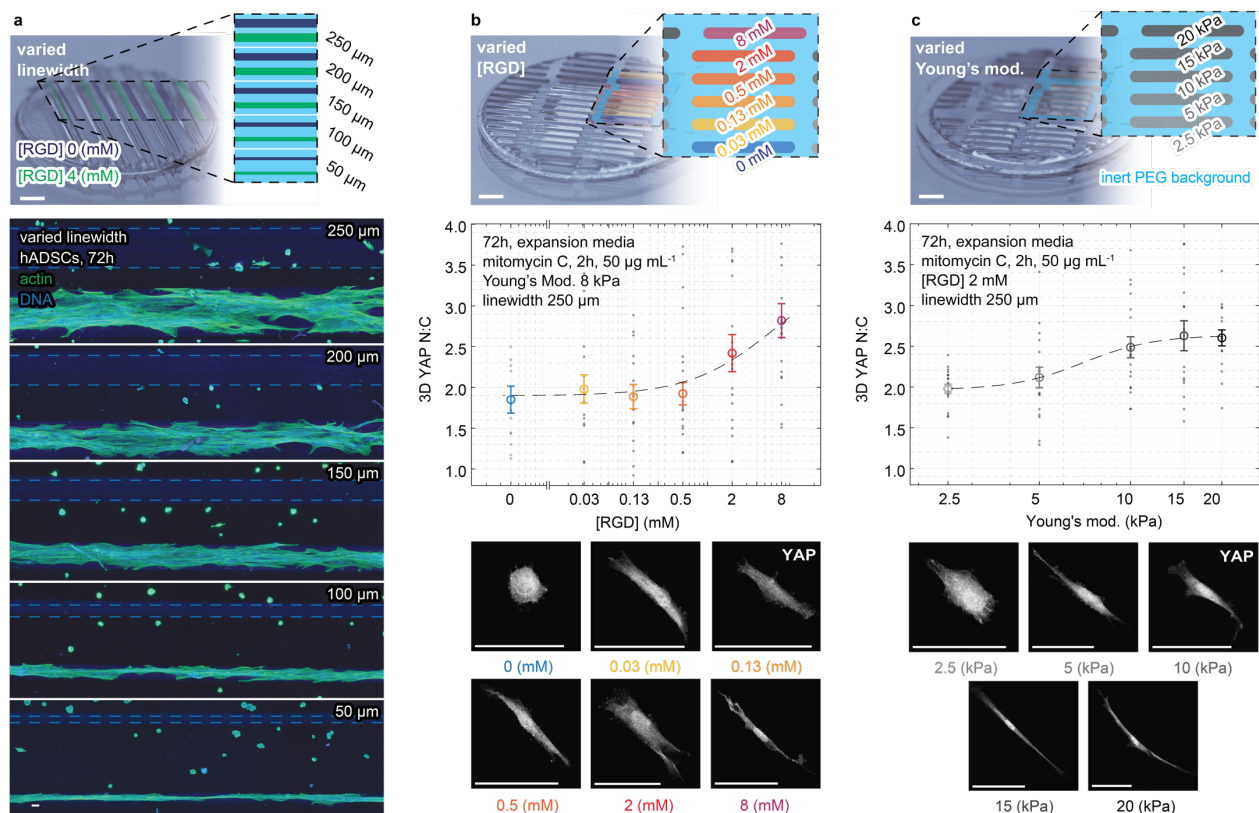

Fig. 2 | Orthogonal programming of niche chemomechanical properties. a-f The effect of CMFL device and photoresin variables on niche Young's modulus (left axis, red) and linewidth (right axis, blue). For each variable subset, an image of the printed niche with streptavidin-FITC conjugate is shown. Gamma correction is applied to subset f for improved visibility. Data points and fit lines on horizontal axes are offset to minimise overlap of concurrently shown dependent variables. Fabrication variables that remain constant are enumerated at the top of each subset. Scale bars, 200 μm. **g-i,** The optimised variable state-space showing microproperties achieved. CMFL niches with well-defined properties can be interpolated from the optimised state-space to generate niches with heterogeneous and orthogonal microstructure. **g,** The relationship between the unified photoinitiator-monomer concentration (horizontal axis) and focus (shown in different colours) on Young's modulus and **h,** linewidth. **i,** The effect of photoinitiator-monomer (horizontal axis), Biotin-PEG-SH concentration ('into-page' axis), and focus (shown in different colours) on the bound thiol-ene conjugate. n.s. – $p > 0.05$ by one-way ANOVA with Bonferroni post hoc tests. Mean ± s.e.m.

Niche-guided cell attachment, spreading and mechanosensing

We explored if CMFL niches with specific chemomechanical microstructure could regulate microscale changes to cell functions. To test this, we printed niches with parallel filaments between 50–250 μm, with physiologically moderate Young's modulus of 8 kPa[36] and alternating

6

concentrations of the cell attachment peptide RGD (cyclo(Arg-Gly-Asp-d-Phe-Cys)) (**Fig. 3a, Table S1**). We then cultured multipotent primary human adipose-derived stromal cells (hADSCs) for 72h on these CMFL niches. Cells attached only to the microstructured regions containing the RGD peptide, with increases to cell spreading over structures with larger linewidths. We then explored if niche RGD properties could be varied to regulate cell attachment and spreading in a dose-dependent fashion. Accordingly, we printed niches with six differing concentrations of RGD between 0–8 mM, and a fixed moderate Young's modulus (8 kPa) and a fixed linewidth (250 µm) (**Fig. S10, Table S1**), observing that cell attachment was correlated to the underlying microstructured RGD concentration.

This result led us to postulate that niches with varied biochemical and mechanical microstructure could regulate more complex cell functions, including microscale changes to cell mechanosensing. To test this, we studied the cellular mechanostat YAP/TAZ, a widely explored marker for determining cellular mechanosensing within multipotent stromal cells[14,37–39]. As previously used, we printed niches with varied RGD, as well as niches with five different microstructured Young's moduli of 2.5-20 kPa, ranging from physiologically soft-to-stiff (**Fig. 3c, Table S1**)[36]. We measured cell mechanosensing by quantifying the relative distribution of YAP/TAZ in the cytoplasm (C) and the nucleus (N) by assessing the N:C ratio of average fluorescent intensity in these two intracellular compartments. Consistent with mechanobiological study of cell-material interactions, the YAP N:C ratio revealed that mechanosensing of hADSCs can be regulated through microstructured chemomechanical (RGD, **Fig. 3b**, Young's moduli, **Fig. 3c**) properties of CMFL generated niches[37–39]. Therein cell mechanosensing exhibited a sigmoidal response to changes in the microstructured concentration of RGD, and Young's modulus. A lower threshold of YAP N:C correlated with a low concentration of RGD and soft Young's modulus, while for high concentrations of RGD and stiff Young's modulus, an upper of YAP N:C was observed. Thus, in this novel demonstration, we show orthogonally programmed niche chemomechanics can achieve microscale spatial regulation of cell mechanosensing. This capability has significant implications for generating tissue *ex vivo*, as YAP signalling plays an important role during development as a critical juncture in Hippo pathway signalling of cell fate decisions, tissue patterning and organ growth[40].

7

Fig. 3 | Niche-guided cell attachment, spreading and mechanosensing. a, Printed line-pairs with 4 or 0 mM RGD, from 50–250 μm, with a fixed Young's modulus of 8 kPa. Representative confocal image shows actin (phalloidin, green) and nucleus (DAPI, blue). Gamma-correction has been applied to improve visibility of the zero RGD concentration dark blue filaments where no cells attach. CMFL niche arrays with varied b, chemical (RGD) and c, mechanical (Young's modulus) properties are shown alongside the quantification and representative images of the 3D nuclear (N) to cytoplasmic (C) ratio of biomolecular mechanostat YAP in hADSCs at 72h as imaged on respective microstructures. Mean ± s.e.m. Scale bars, 50 μm, except macro lens images of CMFL arrays at figure top = 1 mm.

Engineering a tissue construct from a single cell source form orthogonally programmable chemomechanical niche cues.

Given the upstream role of cellular mechanosensing in cell fate decisions[37], we tested if cell fate decisions could be spatially guided by chemically (RGD peptide) and mechanically (Young's modulus) orthogonal microstructured niches. Harnessing the propensity of osteogenic and adipogenic differentiation of the multipotent stromal cells[14,38,41], we sought to generate a bone-fat osteon structure by optimised niche chemomechanics. We assessed osteogenesis by measuring the nucleocytoplasmic (N:C) ratio of RUNX2, an essential transcriptional regulator of osteogenesis coupled with the commitment of multipotent stromal cells to the osteoblast lineage[42], and by visualizing mineralized bone deposition by Alizarin Red staining. Enhanced osteogenesis, revealed by elevated RUNX2 N:C ratio and enhanced mineralisation was correlated with increasing concentrations of RGD (**Fig. 4a,b**) and stiffer Young's modulus (**Fig. 4c,d**). Adipogenesis, assessed as the volumetric ratio of fat to total cytoplasmic volume (**Fig. 4e,f**) was also correlated with mechanically soft (Young's modulus) or peptide-enriched (high RGD) regions of the

8

microstructured niches. The highest fat-cytoplasmic volumetric ratio was associated with mechanical microstructures with 8 mM RGD and a low Young's modulus (with ~7-fold increase at 2.5 kPa relative to 20 kPa). Further, we tested if niches could be orthogonally structured with the morphogen BMP2, that is known to influence osteogenesis. We printed niches with microstructured concentrations of BMP2 (**Fig. 4 g,h**). Assays for osteogenesis showed that RUNX2 N:C scaled up with BMP2 concentration up to 200 ng mL^{-1}, but decreased at 1000 ng mL^{-1}. Interestingly, mineralization was enhanced across same range of microstructure properties (linewidth 250 μm, Young's modulus 8 kPa, RGD 2 mM and BMP2 0 ng mL^{-1}) and did not correlated with the extent of RUNX2 activity.

We next sought to engineer multilineage cell differentiation and generate a structured microtissue from a single cell source. To elicit concurrent cell differentiation of hADSCs to both osteo-and-adipogenic lineages, we generated a microstructured cell niche with properties that reflect the optimal niche microproperties previously explored for osteo-and-adipogenic differentiation **(Fig 4. a-h).** Therein a centralised adipogenic region is surrounded peripherally by an osteogenic region (**Fig. 4i**). hADSCs were seeded over the bone-fat niche and cultured in a 1:1 adipogenic:osteogenic media for 14 days, displayed concurrent osteogenesis (COL 1A-expressing, **Fig. 4j**) and adipogenesis (high lipid content, **Fig. 4j**) in their respective spatial domain (**Fig. 4k, Fig. S11**). Adipogenesis was localised to the centre of the culture, over the region of low stiffness and high RGD, with enhancing osteogenesis towards the region with high stiffness, BMP2 and RGD at the periphery of the microstructure. This experiment showed that the chemomechanical attributes of the microstructured niche can influence cell fate decisions and generate tissue-like multilineage entities.
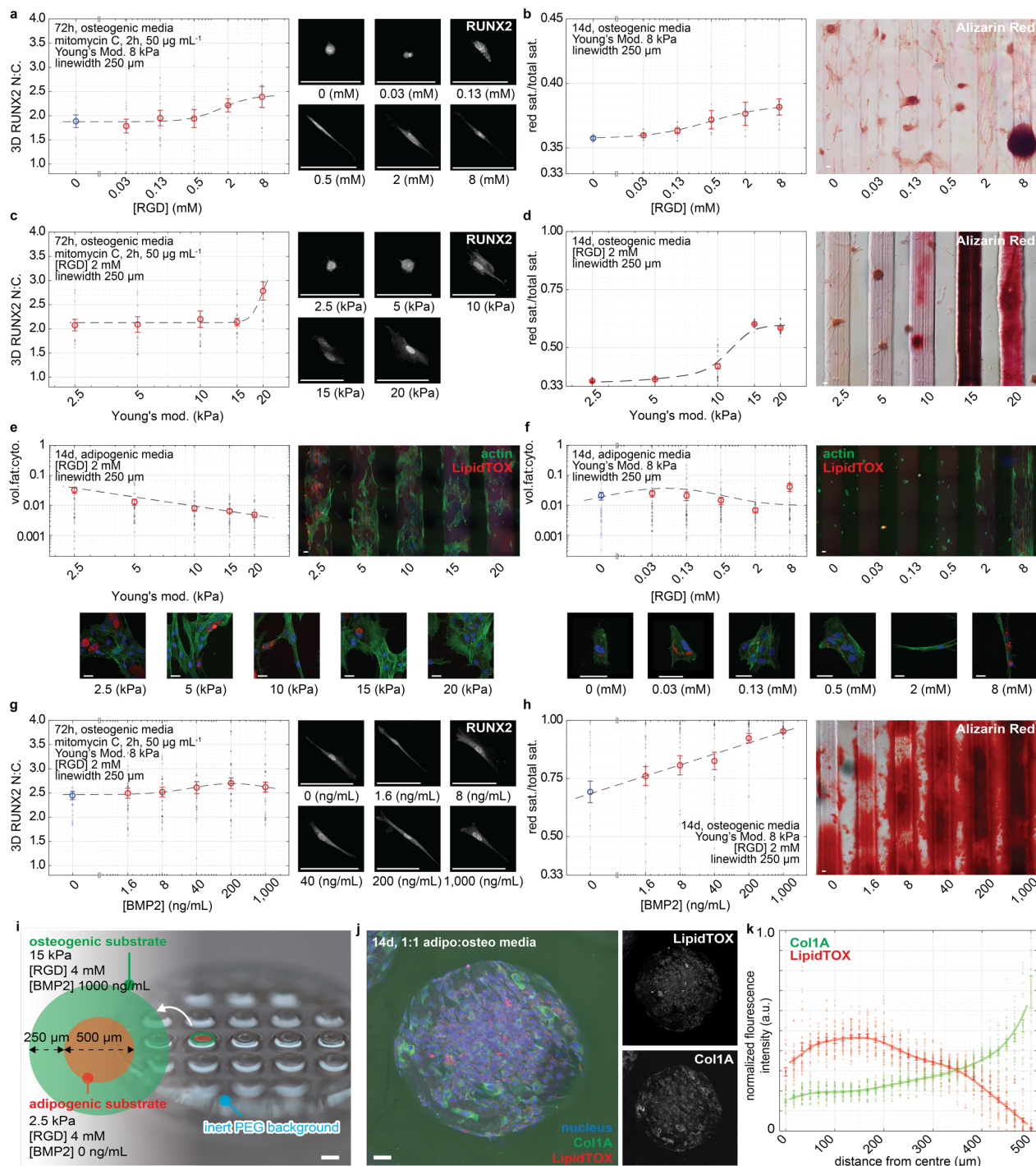
9

Fig 4 | Engineering a tissue construct from orthogonally programmable chemomechanical niche cues. a,b, Osteogenic differentiation of hADSCs on chemically (RGD) microstructured niches. a, Immunofluorescent staining, imaging and quantification of RUNX2 and b, quantification and representative widefield images of Alizarin Red stained bone mineralization. c,d, Osteogenic differentiation on mechanically (Young's modulus) microstructured niches, with RUNX2 and Alizarin Red stains. e,f Adipogenic differentiation over e, mechanically (Young's modulus) and f, chemically (RGD) microstructured niches, with representative max intensity projections and quantification of LipidTOX stained fat volume per cytoplasmic volume (vol. fat:cyto). g,h, Osteogenic differentiation on microstructured concentrations of the bioconjugated morphogen and growth factor BMP2, with RUNX2 and Alizarin Red stains. i-k, Organotypic bone-fat microstructures that mimic the architecture of the osteon with a central adipogenic region and a peripheral osteogenic region. i, Printed CMFL bone-fat niche array with optimised microproperties enumerated j, Representative max intensity projections of CNA35 fluorescent collagen 1A (Col1A) probe and LipidTOX stained hADSCs. The large inset shows nuclear (blue), brightfield (grey), Col1A (green) and LipidTOX (red) channels, beside smaller grayscale insets showing Col1A and LipidTOX channels, gamma corrected for ease of visibility. k, Quantification of the normalized pixel intensity

10

for Col1A and LipidTOX data across replicates. Scale bars 100 μm, except d = 1 mm. Data presented as mean ± s.e.m. throughout. Scale bars 100 μm, except for i = 1 mm.

Niche-guided germ-layer tissue patterning.

We sought to test CMFL for patterning germ-layer tissue derived from pluripotent stem cells[1,43–46]. We build on literature recapitulating gastrulating tissue *in vitro*, with the culture of hiPSCs plated on 200-1000 μm circular adhesive templates[46,47]. As per the predicate work, cell cultured on a homogenous circular template were able to generate radially symmetric germ-layer derivatives (**Fig. S14**). In contrast to culturing cells on a homogenous substrates that were exposed globally to differentiation stimulus, we performed the culture on substrate with heterogeneous niche attributes. We fabricated microstructured niche in squared micropatterns with either uniform-stiffness (**Fig. 5a**), or a one-dimensional gradient of stiffness across the square (**Fig. 5d**). hiPSCs cultured on square microstructures were induced to differentiate with BMP4 (50 ng/mL), into progenitor cells of the mesoderm (BRA-positive), endoderm (SOX17-positive) and ectoderm (SOX2-positive). Quantitative imaging analysis (**Fig. S12**) showed that hIPSCs cultured on uniform stiffness substrate displayed regionalization of germ layer tissues across the centre to the periphery space (**Fig. 5c,j,i,k**), similar to that observed for circular micropatterns[1] (**Fig. S14**). In contrast, cell cultured on substrate of graded stiffness, displayed polarise tissue patterns with BRA- and SOX17-positive cells localised to regions of low stiffness, and SOX2-positive cells to regions with high stiffness (**Fig. 5f,h,l**). The cell types generated in regions of different stiffness matched individually with those on polymeric biomaterials of the comparable level of stiffness[48]. This observation suggests a novel role of niche mechanics in cell-fate choices and the spatial variations in the mechanical property of the niche may underpin the patterning of tissues. These findings are consistent with the notion that protease softening of the basement membrane material plays a role in the patterning of tissues in the anterior-posterior axis of the embryo[49]. Thus, engineering niche microstructures provides an entry point to better understand the mechanisms that underpin spatial patterning of germ layer tissues in stem cell-based embryoid models.
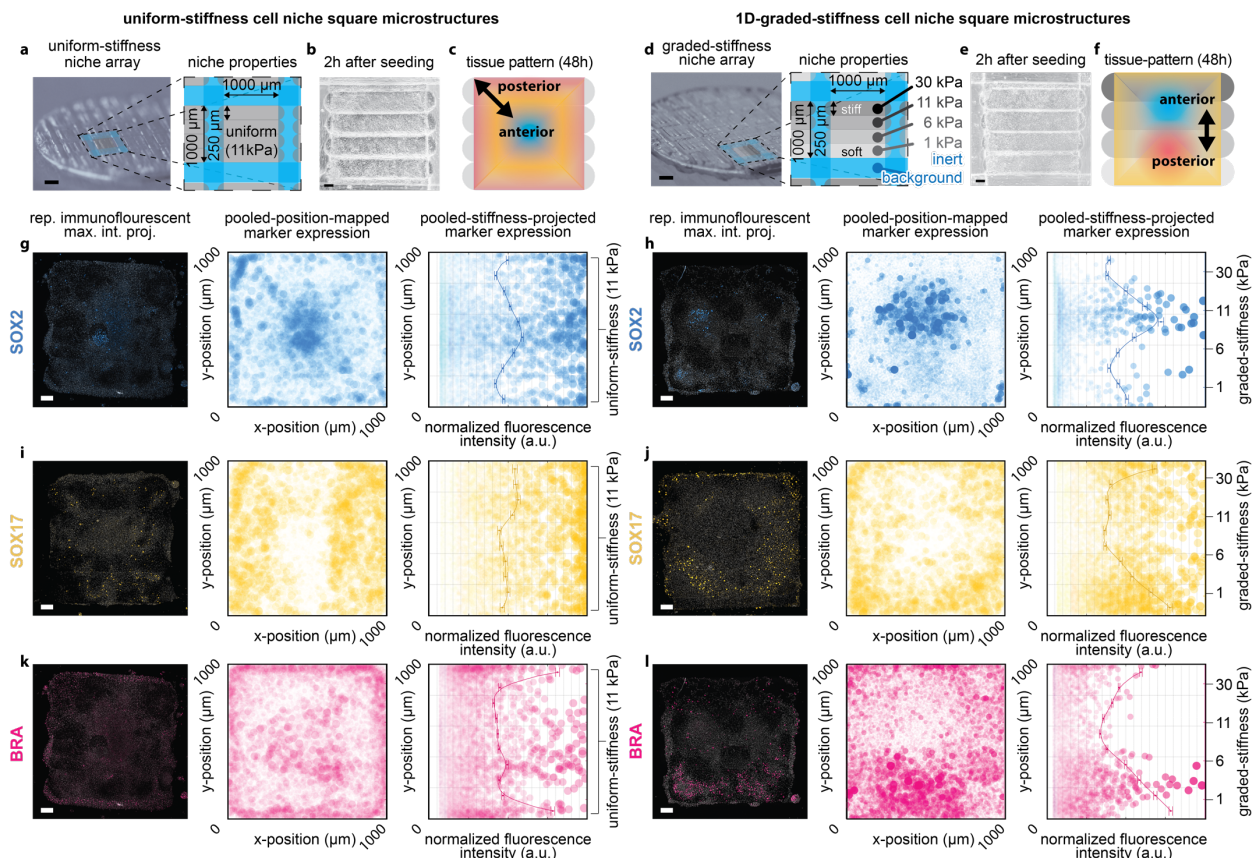
11

Fig. 5 | Niche-guided germ-layer tissue patterning. a,d, Coverslip with CMFL niche arrays showing layout of mechanically microstructured squares. **b,e,** Brightfield imaging at 2h following attachment. **c,f,** schematic summarising germ-layer tissue-patterning of cultures 48h post-BMP4-treatment, showing (mesoderm: BRA, red; ectoderm: SOX2, blue and endoderm: SOX17, yellow). Representative immunofluorescent imaging of cultures on niches with **g,j,k,** uniform-stiffness, or **h,j,l,** graded stiffness. Position-mapped expression graphs of replicate pooled-data is show for each marker to right of immunofluorescent imaging, where each dot represents a single cell with size and transparency linearly correlated to the markers normalized fluorescent intensity. The immunostained data in subsets top **g-l** is gamma-corrected to improve visibility. Scale bars 100 μm, except a,d = 1 mm.

Discussion.

CMFL offers the ability to modulate microscale changes to cell functions through orthogonally programmable chemomechanical niche cues. While both 2D and 3D multi-layer hydrogels can be fabricated using the CMFL method (Fig. 1), we validated the technology capacity of niche-guided cell functions using single-layer (2D) hydrogels. We showed that such niche properties can elicit cell mechanosensing, drive differentiation of stem/progenitor cells tissue, and generate spatially reproducible multilineage tissue models. Future work using CMFL may extend to multi-layer CMFL hydrogels of increased complexity. In such work, the fabrication of multi-layer CMFL hydrogels could be achieved by using chemical photoabsorbers for the facile photolithographic printing of 3D structures[50] or alternatively, using multiphoton lithography of 3D materials. In particular, as multiphoton photolithography can achieve subdiffraction-limited resolutions[26], combining multiphoton methods with FL may enable printing of materials with nano-structured niche properties.

12

Further advancement to the CMFL method could be made by adapting a more specific conjugation chemistry. In particular, our method is limited when conjugating relatively complex macromolecules with numerous cysteine sites. Under these conditions, thiol-ene conjugation occurs stochastically and can lead to the loss of function of the bioconjugate. This limitation has been addressed with more reproducible chemistries including enzymatic methods[30] and specific high affinity non-covalent binding chemistries[51]. Further, such complex chemistries have been demonstrated with multiphoton photolithographic techniques[34].

The CMFL method complements recent research in pluripotent stem cell biology generating complex organoid systems[2,3]. To date, these methods have relied on "self-organization" of cells and tissues in relatively homogeneous niches[52], with microfluidically introduced morphogen patterning[5], or the concurrent extrusion printing of different cell types[3,18,53]. The CMFL method addresses the limitation of relying on the stochastic process in lineage differentiation and morphogenesis of tissue constructs, embryoids and organoids. The CMFL method potentiates the next generation of reproducible synthetic tissue models, wherein tissue architecture is defined through niche-mediated chemomechanical interactions. Applying the CMFL method, it is feasible to reproducibly generate a bone-fat microtissue and polarised embryoid. The CMFL method therefore provides new tools for the investigation of how complex structure and function emerge; how the shape, size and body coordinates of an organism are determined; and more specifically, how mechanical and positional morphogenetic cues works in concert with morphogens and lineage determinant in physiologically functional tissues *ex vivo*.

13

Methods.

Custom built CMFL 3D printer. The 3D printer was built modifying a Hyrel System 30M. Custom components were added including, 405 nm/500 mW laser module and Arduino-based controller electronics, collimating and focusing lens (thorlabs AL1225H and Olympus x10 Plan NA 0.3 160/0.17), a pinhole/ring-actuated iris diaphragm (thorlabs SM1D12D), and hydrophobic print chamber. All custom components of this system are detailed in the supplementary information.

Microstructured niche print chamber. Photoresin is injected into a glass print chamber with a PDMS coated glass slide top and acrylate functionalized coverslip base (Fig. S2). The acrylate-modified glass coverslip base provides a stable surface on which microstructures are covalently attached when printed. Covalent binding between sample and coverslip prevents sample delamination, sample-folding or strain deformation due to hydrogel swelling, as well, the covalent attachment assists sample handling for cell culture and downstream characterisation. To acrylate coverslips, a silanization solution was prepared. In fume hood, a glass dish was filled with methanol (Sigma 322415) and bath sonicated for 5 minutes. The dish was then dried then rinsed a further x2 with methanol. 100 mL of methanol was added to the dish along with 5 mL of glacial acetic acid (Sigma A6283) and 3 mL 3-(trimethoxy silyl) propyl acrylate (TCI A1597). Circular glass coverslips were then washed x3 times in methanol in the glass dish, and silanization solution added before covering the dish to prevent evaporation or contamination from ambient H2O. Coverslips are left for 1 h for silanization to proceed. Following the reaction, coverslips were rinsed x3 in ethanol, wiped clean and dried with N_2. PDMS coating of glass slides was used at the top of the print chamber to prevent the bonding and tearing of photopolymerized microstructured niche samples. PDMS (Corning Sylgard 184) is prepared as 10 parts base, to 1 part curing agent, mixed and then centrifuged to remove bubbles. Slides (Sigma CLS294775X50) are coated on Laurell EDC 650 series spin coater. PDMS is poured onto the top of the samples at approximately the volume of an Australian 50 cent piece. The spin coater is then ramped to 1600 rpm for 10 s and stopped. The glass slides are then placed onto a hot plate at 200 ˚C for 1 min and left to rest while the remaining slides processes in the batch are completed, before being transferred to a 37 ˚C oven overnight.

Measurement of niche microproperties. Microstructured niches were fabricated on acrylated coverslips using the geometries, photoresin and printer variables as reported. The measurement of Young's modulus via force spectroscopy was completed using a JPK NanoWizard Sense AFM, mounted on Nikon Ti microscope. The device was fitted with the SuperCut quartz cantilever holder for liquid immersion and used with Bruker MLCT pyramidal cantilevers with stiffness calibrated

14

370   using the thermal noise method. For force-displacement curve generation, hydrogel samples and AFM cantilever were submerged in x1 PBS. The cantilever approach velocity was fixed to 0.5 µm sec^{-1} and terminated at a threshold force of 10 nN. Measurements were taken from 3 independent experimental replicates from at least 4 different printed-niche-replicates in each experiment. The Young's modulus was calculated from each force-displacement approach curve using a custom

375   fitting program written in MATLAB, with automated contact point determination and fitting for an 18° half-angle conic section (Sneddon model, as per Bruker recommendation for MLCT pyramidal cantilevers), with sample thicknesses bottom effect cone correction as per Gavara et al.[54]. Data for force spectroscopic curves of AFM tip displacement vs indentation force were rejected when discontinuities in the curves were present, corresponding to samples slipping and thus an inaccurate

380   indentation. For the sample shown in Fig. 1d-g only 2 independent experimental replicates were fabricated, as this sample only served to illustrate how a 3D chemomechanically structured material could be fabricated with the CMFL methodology. One replicate was mounted for confocal microscopy (Fig. 1d, e), and the other analysed with force spectroscopy (Fig. 1e, f). Microstructured linewidth and bioconjugation was measured using confocal microscopy.

385   Linewidth was directly measure using Fiji-ImageJ across 3 independent experimental replicates with quantification of the concentration of Biotin-PEG-SH was measured indirectly by measuring the relative fluorescence of bound streptavidin-FITC. Indirect measurement was used to prevent the photobleaching or free radical attack of fluorescent molecules during photopolymerization, that otherwise limited interpretation.

390   **Interpolation method for microstructuring niches chemomechanical properties.** Empirical data was tabulated pairing dependent and independent variables, including Young's modulus, linewidth and the concentration of bioconjugate (**Fig. 2g-i**), with the monomer–photoinitiator ("PEG/PI" below), focus (shown as "Z") and [Biotin-PEG-SH]. Using MATLAB (2020a), we then calculated the value of the independent fabrication variables of PEG/PI and Z after substitution of

395   the desired Young's modulus ($E_{des.}$) and linewidth ($W_{des.}$) as per Equation 1 below:

$$0 = \left(\frac{E_{des.} - \frac{\sum(\tau * E_{em.})}{\sum \tau}}{E_{des.}}\right)^2 + \left(\frac{W_{des.} - \frac{\sum(\tau * W_{em.})}{\sum \tau}}{W_{des.}}\right)^2, where \; \tau = \frac{1}{0.1\sqrt{2\pi}} e^{-\frac{1}{2}\left(\frac{\left|\frac{PEG/PI_{em.} - PEG/PI}{40}\right| + \left|\frac{Z_{em.} - Z}{6}\right|}{0.1}\right)} \; Equ.$$

(1)

where, $PEG/PI_{em.}$ and $Z_{em.}$ are vectors from the independent paired variables from the tabulated empirical dataset presented in **Fig. 2g,h**, and are used to calculate the vector τ that is substituted

400   into Equ. 1, where a solution is obtained for the dependent paired variables $E_{em.}, W_{em.}$. The numbers 40 and 6 in Equ. 1 represent the normalization range for PEG/PI and Z respectively over

15

which data is interpolated. Equ. 1 is solved using the Nelder-Mead simplex method for finding the minimum of unconstrained multivariable functions. The relationship between PEG/PI is calculated as the positive real solution of Equ 2.

405

$$0 = \left| \left(\frac{PEG/PI - 50}{40} \right)^2 + \left(\frac{PI - 0.5}{0.35} \right)^2 \right| - 1 \text{ Equ. (2)}$$

Cell culture. hADSCs (Life Technology) were cultured in expansion media: MesenPRO RS™ Basal Medium (Invitrogen) with the supplement of 2 mM l-glutamine and MesenPRO RS Growth Supplement (Life Technology). hADSCs at passage 3 were used for all the studies. For culture on microstructured niches, a 10 mm coverslip with printed niche arrays was placed in a 48-well plate.

410 The niche arrays were washed twice with PBS before 12 mins UV-light sterilisation using a biosafety cabinet. Medium was changed every 3 days except for studies examining YAP and RUNX2 nuclear translocation, where hADSCs were treated with mitomycin (10 µg mL^{-1}) (Cayman Chemical, 11435) for 2 h, to inhibit proliferation, 24 h after seeding, after which media was replaced with expansion media. For YAP and RUNX2 translocation studies, cells were seeded at

415 3,000 cells cm^{-2}. For differentiation studies cells were seeded at 6,000 cells cm^{-2}, osteogenic (Gibco, A1007001) and adipogenic media (Gibco, A1007201) were used as noted. Experiments using iPSCs were performed with the CRL2429 C16 hiPSC line derived at Australian Institute for Bioengineering and Nanotechnology (AIBN) in university of Queensland as previously described[55]. For routine passaging, cells were passaged with ReLeSR™ and grown on Stem Cell

420 Grade Matrigel® (Croning) coated 6-well plate. All experiments used mTeSR™ plus, with supplements as listed. Fabrication of Matrigel containing microstructured niches were completed within a cold room at 4 °C using the geometries, photoresin and printer variables as reported. For culture on microstructured niches, a 10 mm coverslip with printed niche arrays was placed in a 48-well plate. The niche arrays were washed twice with PBS before 12 mins UV-sterilisation using a

425 biosafety cabinet. C16 hiPSC cells were dissociated with Accutase (Gibco), and pipetted into a single cell suspension in mTeSR™ plus with 10 µM Rock-inhibitor Y27632 (Ri) at 3.3M cells mL^{-1} before seeding at 300 µL per well. After 2h, media was replaced with 10 µM Ri for 10h, before 48h differentiation in 500 µL mTeSR™ plus supplemented with 50 ng mL^{-1} BMP4 (PHC9534 Gibco). For all cell culture experiments, a minimum of 3 independent experimental replicates were

430 completed for each printed fabrication condition and relevant stain. All cells tested negative for mycoplasma contamination. For hADSCs routine PCR assay checks (LookOut® Mycoplasma qPCR Detection Kit, MP0040A-1KT) were completed for mycoplasma contamination, for hiPSC mycoplasma was tested using fluorescent kit (MycoAlertTM Mycoplasma Detection Kit, Catalog #: LT07-318).

16

435 **Immunocytochemistry, confocal imaging and image quantification.** For immunostaining, all solutions, with the exception of those with dilute antibody and fluorophores were syringe filtered through 0.22 μm membrane filters (Merck Millipore SLGP033RS). Cells were fixed at room temperature 4% PFA in x1 PBS buffer for 10 mins and then washed three times with PBS, followed by 12 min permeabilization at room temperature with 0.1 w v^{-1} % Triton X-100 in PBS. Samples

440 were then incubated in a blocking buffer of 3% BSA, 3.75 mg mL^{-1} glycine and 0.05% w v^{-1} Tween 20 in PBS for 1 h at room temperature. Primary antibodies were diluted in 1% BSA and 0.05% w v^{-1} Tween 20 in PBS and added overnight at 4°C (anti-YAP (1:250; Santa Cruz sc-101199), anti-RUNX2-AF488 (1:250; Santa Cruz sc-390351)), or for 2h ((1:400) SOX2, CST #3579; (1:300) SOX17, R&D systems, AF1924; (1:300) BRA, R&D systems, AF2085). For indirect

445 immunostaining, samples were washed x3 times with PBS, and incubated for 2 h at room temperature with corresponding secondary antibody (YAP with Santa Cruz CFL 488 (1:250, sc-516176), SOX2 with ab150075, SOX17 and BRA with ab150077). Nuclear and/or actin counterstains were performed using Abcam iFluor conjugated phalloidin (ab176753, ab176759), and Hoechst 33342 at 0.1 μg mL–1 (Sigma, 14533) dilute in x1 PBS and incubated for 30 mins at

450 room temperature. Following counterstain incubation, samples were washed an additional x3 with PBS containing 0.05% w v^{-1} % sodium azide. All microstructured niche samples were mounted in PMMA blocks with a recessed circular hole to avoid damaging samples (**Fig. S9**). For YAP and RUNX2 translocation studies, microscopy was completed on a Zeiss LSM 800 Confocal microscope using 63x Objective Plan-Apochromat 63x/1.40NA Oil objective (with in-plane lateral

455 resolution of 0.413–0.124 μm per pixel) and pinhole diameter of 1.0 AU (50.34 μm) and azimuthal resolution of 0.4 μm. Nuclear images from Hoechst staining were used to creates masks that define nuclear volume, and cytoplasmic masks were defined from flood-filled phalloidin stains, with the average fluorescent intensity of each volume calculated in MATLAB. Therein, the YAP/RUNX2 nuclear to cytoplasmic translocation ratio was determined as the ratio of the mean YAP/RUNX2

460 fluorescent saturation intensity of the nuclear volume divided by the fluorescent saturation intensity in the non-nuclear cell cytoplasmic volume. In Fig. 3b,c, 4a,c, YAP/RUNX2 measurements of a total of at least 12 single cells per condition were pooled across 3 independent experimental replicates from at least 4 printed-niche-replicates. Representative images were selected according to their proximity to the mean data as calculated across all replicates. For imaging hiPSCs over 1

465 mm square microstructures, we used a 10x Nikon A1R confocal microscope with an in-plane lateral resolution of 0.615 μm per pixel (2048x2048 pixels), and an azimuthal resolution of 2.5–3.3 μm. Using Hoechst nuclear marker, individual cell nuclei were segmented using Trainable Weka Segmentation, defining three different pixel classes, including: nuclear-contours, nuclei, and

17

470 background. Probability maps were generated and used to identify individual cell nuclei with a loss function that assigns pixels to the final nuclei mask given they: have at least 50% chance of being a nuclei and at most a 66% and 75% chance of being a pixel belonging to the nuclear-contour and background pixel-classes respectively. Using the nuclei masks the mean fluorescent intensity for each channel and nuclei was calculated. Then with the respective coordinates of each mask, the coordinates of each nuclei within the microstructures was calculated. This allowed replicate data

475 to be remapped to a single plot that showed the average position mapped immunostained expression of the 3 germ layer channels with marker-size and marker-opacity changing proportionally to the fluorescent intensity of the nuclei (see SI for additional details). The expression maps in Fig. 5b,c pool data from 3 independent experimental replicates, analysing at least 15 printed-niche-replicates in total and >101,594 individual cells for each marker analysed.

480 **LipidTOX, CNA35 and Alizarin Red staining of ADSC differentiation.** We assayed the differentiation of hADSCs toward adipogenic and osteogenic lineage in response to niche microproperties. All solutions listed below were syringe filtered through 0.22 µm membrane filters (Merck Millipore SLGP033RS). Alizarin Red (Sigma, A5533) staining was performed to examine the presence of mineralized deposits under osteogenic differentiation conditions. Samples were

485 washed x2 with PBS before fixation at room temperature in 4% PFA dilute in x1 PBS buffer for 10 mins and then washed three times with PBS. Samples were then washed x3 in Milli-Q H2O before incubation with Alizarin Red stain for 5 minutes (9.6 mg mL–1 Alizarin Red at a pH of 4.2, adjusted with acetic acid). Following Incubation, samples were washed x5 with Milli-Q H2O, followed by a further x3 washes with x1 PBS containing 0.05 w v–1 % sodium azide. We examined

490 cell mineralization with Alizarin Red staining and widefield Colour microscopy of materials following 14 d of culture. Cells were imaged using a Nikon Ni E microscope with colour DS-Fi2 camera and Plan Apo Lambda 10x/0.45NA dry objective. The localization of osteogenesis over specified RGD and Young's modulus regions was quantified for each niche-replicate sample as the ratio of the mean red saturation divided by the mean total saturation that combines red, green and

495 blue colour components for corresponding region of interest. For Alizarin Red Stains in Fig. 4 b,d,h,k, measurements were pooled across 3 independent experimental replicates from at least 4 printed-niche-replicates in each experiment for a total of at least 12 total measurements per niche condition. Staining with LipidTOX Red Neutral Lipid Stain (Thermo H34476) was completed to assess quantify cell fat volume under adipogenic differentiation conditions. Samples were fixed at

500 room temperature 4% PFA in x1 PBS buffer at pH 7.4 for 10 mins and then washed three times with PBS, followed by 12 min permeabilization at room temperature with 0.1 w v–1 % Triton X-100 in PBS. Samples were then incubated with LipidTOX Red Neutral Lipid Stain (diluted 1:800),

18

Abcam iFluor conjugated phalloidin (1:200), and Hoechst 33342 at 0.1 µg mL–1 (Sigma, 14533) dilute in x1 PBS for 30 mins at room temperature. For LipidTOX data in Fig. 4 e,f, measurements were pooled across 3 independent experimental replicates from at least 4 printed-niche-replicates in each experiment for a total of at least 24 fields-of-view per niche condition. In Fig. 4 k, LipidTOX measurements were pooled across 3 independent experimental replicates from at least 4 printed-niche-replicates in each experiment for a total of 12 organotypic bone-fat niches. Following incubation, samples were washed an additional x3 with x1 PBS containing 0.05 w v–1 % sodium azide. Fluorescent microscopy of large fields of view (arrays of RGD and Young's modulus) were tiled using a Nikon Ni E microscope with motorised stage and monochrome DS-Qi2 camera and Plan Apo Lambda 10x/0.45NA dry objective. Confocal microscopy was completed on a Zeiss LSM 800 Confocal microscope using x63 Objective Plan-Apochromat 63x/1.40NA Oil objective (with in-plane lateral resolution of 0.413 µm per pixel), pinhole diameter of 1.0 AU (50.34 µm) and azimuthal resolution of 0.4 µm. Segmentation was performed using custom MATLAB scripting that makes use of the open microscopy Bio-Formats tool. Masks were created to define cytoplasmic and fat volumes using phalloidin and LipidTOX stains. For production and purification of the fluorescent collagen 1A probe, pET28a-EGFP-CNA35 plasmid was received as a gift from Maarten Merkx (Addgene plasmid # 61603; http://n2t.net/addgene:61603; RRID: Addgene_61603) and synthesized as reported previously[56]. In brief, protein yields of the CNA35 probe were synthesised using E.Coli bacteria, before purification using ÄKTApurifier (Cytiva) and a 5 ml Ni-NTA Superflow Cartridge (Qiagen), dialysis with SnakeSkinTM Dialysis tubing with 10 kDa MWCO, and concentration with an Amicon 10 kDa MWCO centrifugal filter unit. For imaging, 0.5 µM of EGFP-CNA35 solution were added to the sample and incubated on a plate rocker for 15 mins, before washing twice with PBS. In Fig. 4 k, Col1A measurements were pooled across 3 independent experimental replicates from at least 4 printed-niche-replicates in each experiment for a total of 12 organotypic bone-fat niches.

19

and Dr Neftali Flores-Rodriguez. PN thanks Karl Gifford for his assistance with modification and operation of the custom Hyrel System 30M.

Competing Interests statement. No competing interests are declared by the authors.

Code availability statement. No standalone software or software tools were developed for this

560   work. However, all scripts used for data analysis are available upon request to the corresponding authors.

Data availability statement. Datasets supporting the conclusions are shown within the article and its additional files. Data and corresponding scripts with sample data for analysis are available upon

565   request to the corresponding authors.

References.
1. Warmflash, A., Sorre, B., Etoc, F., Siggia, E. D. & Brivanlou, A. H. A method to recapitulate

570   early embryonic spatial patterning in human embryonic stem cells. *Nat. Methods* **11**, 847 (2014).

20

2. Nikolaev, M. *et al.* Homeostatic mini-intestines through scaffold-guided organoid morphogenesis. *Nature* (2020) doi:10.1038/s41586-020-2724-8.

3. Brassard, J. A., Nikolaev, M., Hübscher, T., Hofer, M. & Lutolf, M. P. Recapitulating macro-scale tissue self-organization through organoid bioprinting. *Nat. Mater.* (2020) doi:10.1038/s41563-020-00803-5.

4. Manfrin, A. *et al.* Engineered signaling centers for the spatially controlled patterning of human pluripotent stem cells. *Nat. Methods* **16**, 640 (2019).

5. Zheng, Y. *et al.* Controlled modelling of human epiblast and amnion development using stem cells. *Nature* **573**, 421–425 (2019).

6. Birey, F. *et al.* Assembly of functionally integrated human forebrain spheroids. *Nature* **545**, 54–59 (2017).

7. Engler, A. J., Sen, S., Sweeney, H. L. & Discher, D. E. Matrix elasticity directs stem cell lineage specification. *Cell* **126**, 677–689 (2006).

8. Cameron, A. R., Frith, J. E. & Cooper-White, J. J. The influence of substrate creep on mesenchymal stem cell behaviour and phenotype. *Biomaterials* **32**, 5979–5993 (2011).

9. Dalby, M. J., Gadegaard, N. & Oreffo, R. O. Harnessing nanotopography and integrin–matrix interactions to influence stem cell fate. *Nat. Mater.* **13**, 558–569 (2014).

10. Khetan, S. *et al.* Degradation-mediated cellular traction directs stem cell fate in covalently crosslinked three-dimensional hydrogels. *Nat. Mater.* **12**, 458 (2013).

11. Hosaka, S., Ozawa, H. & Tanzawa, H. Controlled release of drugs from hydrogel matrices. *J. Appl. Polym. Sci.* **23**, 2089–2098 (1979).

12. Edelman, E. R., Mathiowitz, E., Langer, R. & Klagsbrun, M. Controlled and modulated release of basic fibroblast growth factor. *Biomaterials* **12**, 619–626 (1991).

13. Burdick, J. A. & Anseth, K. S. Photoencapsulation of osteoblasts in injectable RGD-modified PEG hydrogels for bone tissue engineering. *Biomaterials* **23**, 4315–4323 (2002).

14. Cosgrove, B. D. *et al.* N-cadherin adhesive interactions modulate matrix mechanosensing and fate commitment of mesenchymal stem cells. *Nat. Mater.* **15**, 1297 (2016).

15. Miller, J. S. *et al.* Rapid casting of patterned vascular networks for perfusable engineered three-dimensional tissues. *Nat. Mater.* **11**, 768–774 (2012).

16. Xu, T. *et al.* Complex heterogeneous tissue constructs containing multiple cell types prepared by inkjet printing technology. *Biomaterials* **34**, 130–139 (2013).

17. Hockaday, L. *et al.* Rapid 3D printing of anatomically accurate and mechanically heterogeneous aortic valve hydrogel scaffolds. *Biofabrication* **4**, 035005 (2012).

21

18.   Kolesky, D. B., Homan, K. A., Skylar-Scott, M. A. & Lewis, J. A. Three-dimensional bioprinting of thick vascularized tissues. *Proc. Natl. Acad. Sci.* **113**, 3179–3184 (2016).

19.   Kang, H.-W. *et al.* A 3D bioprinting system to produce human-scale tissue constructs with structural integrity. *Nat. Biotechnol.* **34**, 312–319 (2016).

20.   Ober, T. J., Foresti, D. & Lewis, J. A. Active mixing of complex fluids at the microscale. *Proc. Natl. Acad. Sci.* **112**, 12293–12298 (2015).

21.   Skylar-Scott, M. A., Mueller, J., Visser, C. W. & Lewis, J. A. Voxelated soft matter via multimaterial multinozzle 3D printing. *Nature* **575**, 330–335 (2019).

22.   Lee, A. *et al.* 3D bioprinting of collagen to rebuild components of the human heart. *Science* **365**, 482 (2019).

23.   Hadden, W. J. *et al.* Stem cell migration and mechanotransduction on linear stiffness gradient hydrogels. *Proc. Natl. Acad. Sci.* **114**, 5647–5652 (2017).

24.   Ma, X. *et al.* Deterministically patterned biomimetic human iPSC-derived hepatic model via rapid 3D bioprinting. *Proc. Natl. Acad. Sci.* **113**, 2206–2211 (2016).

25.   Lawlor, K. T. *et al.* Cellular extrusion bioprinting improves kidney organoid reproducibility and conformation. *Nat. Mater.* 1–12 (2020).

26.   Müller, P. *et al.* STED-Inspired Laser Lithography Based on Photoswitchable Spirothiopyran Moieties. *Chem. Mater.* **31**, 1966–1972 (2019).

27.   Chen, C. S., Mrksich, M., Huang, S., Whitesides, G. M. & Ingber, D. E. Geometric control of cell life and death. *Science* **276**, 1425–1428 (1997).

28.   Mosiewicz, K. A. *et al.* In situ cell manipulation through enzymatic hydrogel photopatterning. *Nat. Mater.* **12**, 1072 (2013).

29.   Luo, Y. & Shoichet, M. S. A photolabile hydrogel for guided three-dimensional cell growth and migration. *Nat. Mater.* **3**, 249 (2004).

30.   Shadish, J. A., Benuska, G. M. & DeForest, C. A. Bioactive site-specifically modified proteins for 4D patterning of gel biomaterials. *Nat. Mater.* 1 (2019).

31.   Yin, H., Ding, Y., Zhai, Y., Tan, W. & Yin, X. Orthogonal programming of heterogeneous micro-mechano-environments and geometries in three-dimensional bio-stereolithography. *Nat. Commun.* **9**, 4096 (2018).

32.   Mayer, F. *et al.* Multimaterial 3D laser microprinting using an integrated microfluidic system. *Sci. Adv.* **5**, eaau9160 (2019).

33.   Dendukuri, D., Pregibon, D. C., Collins, J., Hatton, T. A. & Doyle, P. S. Continuous-flow lithography for high-throughput microparticle synthesis. *Nat. Mater.* **5**, 365 (2006).

22

34. Richter, B. *et al.* Guiding cell attachment in 3D microscaffolds selectively functionalized with two distinct adhesion proteins. *Adv. Mater.* **29**, 1604342 (2017).

35. Fairbanks, B. D., Schwartz, M. P., Bowman, C. N. & Anseth, K. S. Photoinitiated polymerization of PEG-diacrylate with lithium phenyl-2, 4, 6-trimethylbenzoylphosphinate: polymerization rate and cytocompatibility. *Biomaterials* **30**, 6702–6707 (2009).

36. Guimarães, C. F., Gasperini, L., Marques, A. P. & Reis, R. L. The stiffness of living tissues and its implications for tissue engineering. *Nat. Rev. Mater.* 1–20 (2020).

37. Dupont, S. *et al.* Role of YAP/TAZ in mechanotransduction. *Nature* **474**, 179–183 (2011).

38. Yang, C., Tibbitt, M. W., Basta, L. & Anseth, K. S. Mechanical memory and dosing influence stem cell fate. *Nat. Mater.* **13**, 645–652 (2014).

39. Caliari, S. R., Vega, S. L., Kwon, M., Soulas, E. M. & Burdick, J. A. Dimensionality and spreading influence MSC YAP/TAZ signaling in hydrogel environments. *Biomaterials* **103**, 314–323 (2016).

40. Meng, Z., Moroishi, T. & Guan, K.-L. Mechanisms of Hippo pathway regulation. *Genes Dev.* **30**, 1–17 (2016).

41. Chaudhuri, O. *et al.* Hydrogels with tunable stress relaxation regulate stem cell fate and activity. *Nat. Mater.* **15**, 326–334 (2016).

42. Komori, T. Regulation of bone development and extracellular matrix protein genes by RUNX2. *Cell Tissue Res.* **339**, 189 (2010).

43. Muncie, J. M., Ayad, N. M., Lakins, J. N. & Weaver, V. M. Mechanics regulate human embryonic stem cell self-organization to specify mesoderm. *Dev.-CELL--20-00131* (2020).

44. Tewary, M. *et al.* A stepwise model of reaction-diffusion and positional information governs self-organized human peri-gastrulation-like patterning. *Development* **144**, 4298–4312 (2017).

45. Xue, X. *et al.* Mechanics-guided embryonic patterning of neuroectoderm tissue from human pluripotent stem cells. *Nat. Mater.* **17**, 633–641 (2018).

46. Fu, J., Warmflash, A. & Lutolf, M. P. Stem-cell-based embryo models for fundamental research and translation. *Nat. Mater.* 1–13 (2020).

47. Martyn, I., Kanno, T., Ruzo, A., Siggia, E. & Brivanlou, A. Self-organization of a human organizer by combined Wnt and Nodal signalling. *Nature* **558**, 132–135 (2018).

48. Przybyla, L., Lakins, J. N. & Weaver, V. M. Tissue mechanics orchestrate Wnt-dependent human embryonic stem cell differentiation. *Cell Stem Cell* **19**, 462–475 (2016).

49. Kyprianou, C. *et al.* Basement membrane remodelling regulates mouse embryogenesis. *Nature* 1–6 (2020).

23

670   50.   Grigoryan, B. *et al.* Multivascular networks and functional intravascular topologies within biocompatible hydrogels. *Science* **364**, 458–464 (2019).

51.   Wylie, R. G. *et al.* Spatially controlled simultaneous patterning of multiple growth factors in three-dimensional hydrogels. *Nat. Mater.* **10**, 799 (2011).

52.   Gjorevski, N. *et al.* Designer matrices for intestinal stem cell and organoid culture. *Nature*
675   **539**, 560–564 (2016).

53.   Kolesky, D. B. *et al.* 3D bioprinting of vascularized, heterogeneous cell-laden tissue constructs. *Adv. Mater.* **26**, 3124–3130 (2014).

54.   Gavara, N. & Chadwick, R. S. Determination of the elastic moduli of thin samples and adherent cells using conical atomic force microscope tips. *Nat. Nanotechnol.* **7**, 733 (2012).

680   55.   Briggs, J. A. *et al.* Integration-free induced pluripotent stem cells model genetic and neural developmental features of down syndrome etiology. *Stem Cells* **31**, 467–478 (2013).

56.   Aper, S. J. *et al.* Colorful protein-based fluorescent probes for collagen imaging. *PloS One* **9**, e114983 (2014).

24